PAPER

The effects of sub-bandgap transitions and the defect density of states on the photocurrent response of a single ZnO-coated silica nanospring

IOP Publishing Nanotechnology
Nanotechnology 32 (2021) 035202 (16pp) https://doi.org/10.1088/1361-6528/abbcec

The effects of sub-bandgap transitions and the defect density of states on the photocurrent response of a single ZnO-coated silica nanospring

Peter M Wojcik[1], Lyndon D Bastatas[2], Negar Rajabi[1], Pavel V Bakharev[1] and David N McIlroy[3]

[1] Department of Physics, University of Idaho, Moscow, ID 83844, United States of America
[2] Department of Physics, Western Mindanao State University, Baliwasan, Zamboanga City 7000, Philippines
[3] Department of Physics, Oklahoma State University, Stillwater, OK 74074, United States of America

E-mail: dave.mcilroy@okstate.edu

Received 10 June 2020, revised 28 September 2020
Accepted for publication 30 September 2020
Published 21 October 2020

Abstract

The electrical and optoelectronic properties of nanometer-sized ZnO structures are highly influenced by its native point defects. Understanding and controlling these defects are essential for the development of high-performance ZnO-based devices. Here, an electrical device consisting of a polycrystalline ZnO-coated silica nanospring was fabricated and used to characterize the electrical and photoconductive properties of the ZnO layer using near-UV (405 nm) and sub-bandgap (532 and 633 nm) excitation sources. We observe a photocurrent response with all three wavelengths and notably with 532 nm green illumination, which is the energy associated with deep oxygen vacancies. The polycrystalline ZnO-coated silica nanospring exhibits a high responsivity of 1740 A W^{-1} with the 405 nm excitation source. Physical models are presented to describe the photocurrent rise and decay behavior of each excitation source where we suggest that the rise and decay characteristics are highly dependent on the energy of the excitation source and the trapping of electrons and holes in intermediate defect levels in the bandgap. The energy levels of the trap depths were determined from the photoconductive decay data and are matched to the reported energy levels of singly and doubly ionized oxygen vacancies. A phenomenological model to describe the dependence of the saturation photocurrent on excitation intensity is presented in order to understand the characteristics of the observed breaks in the slopes of the saturation photocurrent versus excitation intensity profile.

Keywords: nanocoils, nanosprings, nanowires, photoconductivity, photocurrent, photodetectors, zinc oxide

(Some figures may appear in colour only in the online journal)

1. Introduction

ZnO has a direct wide bandgap (3.37 eV) and a large exciton binding energy at room temperature (60 meV), which make it an excellent semiconducting candidate for a variety of applications, including UV photodetection [1–5], solar energy conversion [6, 7], chemical sensing [8–11], light emitting diodes [12, 13], and piezoelectric nanogenerators [14]. ZnO is also one of the most promising metal oxide semiconducting materials for photodetection applications due to its non-toxicity, low cost, ability to be easily synthesized [15], and high electron mobility [7]. Many of the aforementioned studies link ZnO's wide bandgap with UV applications; however, applications such as those used for solar energy conversion

require a wide spectral response with photodetection sensitivity in the visible light region. Tuning a pristine one-dimensional ZnO nanowire (NW) photodetector to the visible spectrum has been achieved by surface functionalization with gold nanoparticles [16] and carbon nanodots [17], by doping with Cu [18] and Mn [19], and by creating a core–shell structure consisting of a ZnO NW core and Zn-rich ZnO shell [20]. A visible response has also been observed in ZnO epilayers [21], polycrystalline ZnO [22], ZnO nanocones [23], and thin-film ZnO [4], all of which include a variety of native point defects (NPDs) in the bandgap such as oxygen and zinc vacancies, and zinc interstitials. Successful control of the NPD density in ZnO nanostructures has been achieved through doping, modifying growth conditions [24], and annealing [22, 23]. The high surface-to-volume ratio of ZnO-based nano-architectures, which is vital to the performance of the many applications of ZnO, is also greatly affected by a strong sensitivity to these NPDs. Understanding and controlling of NPDs and how they affect the electrical and optoelectronic properties of ZnO nanostructures is therefore paramount for the optimization of ZnO-based device architectures.

NPDs have been extensively studied via photoluminescence, which has given evidence for an abundance of deep and shallow defect levels arising from several prominent emissions in the red, orange, green, and violet [4, 23, 25–29]. The green emission has been thoroughly reported [23, 25–28], however its origins are still controversial due to the complexity of the analyzation of the photoluminescence spectra arising from the multiple possible donor–acceptor combinations that can match experimental photoluminescence energies. Identifying the origin of the green emission energy level is further complicated by variations in the theoretically calculated depths of the NPD energy levels [30, 31]. The sub-bandgap photocurrent response of a variety of unmodified ZnO structures has been reported [4, 21–23, 27, 32–39]; however, only approximately half of these studies have reported a photocurrent response with green light [4, 23, 27, 32, 35, 37, 38], and even fewer present models for photocurrent generation and recombination from green and other sub-bandgap illumination sources. The dependence of the saturation photocurrent on excitation intensity has also been reported for ZnO-based materials [1, 2, 19, 33, 40–42]. However, to the best of our knowledge, no phenomenological model exists to explain the observed breaks in the slope of the saturation photocurrent versus excitation intensity profile for ZnO.

Here, we report on the electrical and photoconductive properties of a thin ∼70 nm polycrystalline ZnO coating on a silica nanospring (NS) to study how near-UV (405 nm) and sub-bandgap (532 and 633 nm) excitation affects the photocurrent rise and decay response, responsivity, and the excitation intensity dependence of the saturation photocurrent. We observe that the polycrystalline ZnO-coated silica NS exhibits a typical two-step fast and slow rise and decay photocurrent behavior. Despite the two-step rise and decay processes having been well documented in previous literature, there is much debate concerning the predominant underlying physical processes used to describe the rise and decay photocurrent behavior observed for ZnO-based photodetectors [4, 21, 32, 35, 36, 38, 43–49]. It is well known, however, that these photoconductive properties are highly dependent on NPDs and their corresponding energy levels within the bandgap [4, 21–23, 32, 36, 45, 47]. We first provide a review of these NPDs and their interactions with external atmospheric conditions, their behavior as electron (hole) traps, and their sources of sub-bandgap photocurrent generation. We then present physical models to describe the near-UV and sub-bandgap photocurrent rise and decay behavior observed in our experiments. The physical models show that the observed differences in the rate of change in the rise and decay of the photocurrent for each excitation source is highly dependent on the excitation wavelength and the trapping of carriers within the bandgap. Finally, we present a phenomenological model to explain the observed breaks in the slope of the saturation photocurrent versus excitation intensity profile. These results provide a better understanding of the visible photocurrent response in ZnO, which is critical for the advancement of ZnO-based devices and applications that require them to have a wide spectral response.

2. Experimental

2.1. Silica NS growth

Silica NSs were grown on Si/SiO_2 (500 nm thermal oxide) substrates using a modified chemical vapor deposition process previously described by Wojcik *et al* [50] and Wang *et al* [51]. Initially, a ∼5–10 nm thick layer of Au was sputtered onto the Si/SiO_2 substrate, serving as the catalyst for NS growth. The atmospheric pressure and low temperature (350 °C) growth conditions in the initial phases of NS growth facilitates the formation of an asymmetrical Au–Si catalyst shape. Multiple amorphous individual silica NWs ranging in diameters from ∼10 to 20 nm are then formed beneath the catalyst. Variations in the growth rates of the individual silica NWs produces an asymmetry in the interfacial surface tension and hence a variable work of adhesion (contact angle) along the boundary of the catalyst-NW interface. The variable work of adhesion provides the asymmetry necessary for a helical precession of the catalyst that subsequently produces a helical structure. The helical shapes of individual NSs are random and varied; however, the helical shape of an individual NS is usually well-defined for micron-long sections of its free-length. The free-length of individual NSs are on the order of hundreds of microns, and the wire diameter ranges from ∼70 to 500 nm. The growth of NSs on a flat substrate produces a highly dense mat resulting in an area density of ∼1.5 mg of NSs per cm^2 [52].

2.2. ZnO deposition on silica NSs

Following NS growth, a thin ∼70 nm coating of ZnO was applied to the silica NS surface using a custom-built atomic layer deposition (ALD) system [9, 10, 53]. The system

consisted of a tube furnace acting as the reaction chamber, which was operated at 170 °C and used the precursors diethyl zinc (DEZn) and deionized water (DI) as sources of zinc and oxygen, respectively. The ALD cycle began with the system under vacuum at a base pressure of ∼400 mTorr. A 250 ms pulse of DEZn into a 6 sccm flow of Ar pressurized the system to ∼2 Torr. The system was then purged for 2 s with Ar and subsequently returned to the base pressure. An identical cycle was repeated, except for DI in lieu of DEZn, completing the full ALD cycle. The pressurization of the reaction chamber during the DEZn and DI pulses facilitates diffusion into the mat of NSs. A typical ALD process consisted of 150 cycles and produced an average ZnO thickness of ∼70 nm [9, 53].

2.3. Device fabrication

The Si/SiO_2 substrates with ZnO-coated silica NSs (ZnO-NSs) were placed in isopropanol (IPA) and gently agitated with a submersed pipette to suspend individual ZnO-NSs in the IPA. Si/SiO_2 (500 nm thermal oxide) substrates were prepared for photolithography via cleaning sequentially with acetone, IPA, and DI, followed by drying with N_2. A drop-casting method was used to transfer the ZnO-NSs onto the Si/SiO_2 substrates by using a pipette to draw from the solution of ZnO-NSs/IPA and allowing the solution to evaporate on the Si/SiO_2 surface. The drop casting process was repeated until a sufficient quantity of ZnO-NSs were deposited on the Si/SiO_2 substrate. A standard bi-layer photolithography process using LOR3A and SPR220-4.5 photoresist was used to create a pattern of 27 interdigitated electrodes on the Si/SiO_2 substrate. Both resists were manufactured by MicroChem Corporation. The channel length of each interdigitated electrode was ∼12 000 μm to increase the probability of making sufficient contact with a single ZnO-NS. The patterned substrates were coated sequentially with Ti (20 nm) and Au (200 nm) via thermal evaporation to create electrical contacts; then the photoresist and Ti/Au were removed in photoresist remover. A micromanipulator (Micromanipulator Model 110 with Model 7 A probe tip) was used in concert with an Olympus BX51 optical microscope to remove all but one ZnO-NS bridging the electrode gap. The single ZnO-NS device was annealed in a tube furnace at temperatures of 300 °C and 400 °C while continually flowing Ar at a rate of 50 sccm to improve the electrical conductivity between the ZnO-NS and the contacts. The furnace was ramped to the final anneal temperature in 15 min then shut off and allowed to cool for several hours to ∼50 °C. The unannealed and annealed device at 300 °C both displayed current–voltage curves in the dark that were characteristic of a Schottky barrier. Annealing at 400 °C produced an Ohmic response, which is discussed in section 5.1.

2.4. ZnO-NS device and ZnO structural characterization

Electrical measurements were acquired with a Keithley Model 2400 using a two-point probe method with two micromanipulators (Micromanipulator Model 110 with Model 7 A probe tip). The single ZnO-NS device was placed on an Olympus BX51 microscope stage and illuminated with 633 nm HeNe (Melles Griot Model 05-LHR-927), 532 nm (AixiZ Model AD-532-25ADJ), and 405 nm (AixiZ Model AH405-201 230) excitation sources, which were focused on the ZnO-NS with a 10× microscope objective producing a spot size of ∼300 μm. The laser intensity was controlled with a Newport Optics circular variable neutral density filter and measured at the sample with a Thor Labs model PDA36A Si photodetector. The crystal structure of the ZnO coating was characterized with a Siemens x-ray diffractometer D5000 (XRD) using the Cu K_α line and 2° steps ($\lambda = 1.54$ Å). Scanning electron microscopy (SEM) images were obtained with a Zeiss Supra 35 SEM. All electrical and optoelectronic measurements were performed at room temperature and atmospheric pressure.

3. Background on defects, and photoconduction and recombination mechanisms in ZnO

The UV and sub-bandgap photocurrent response of ZnO is more complex than a typical band-to-band photocurrent response because of the characteristic long rise and decay behavior which are indicative of long electron lifetimes arising from photocurrent generation and recombination processes due to the various NPD types and their corresponding energy levels within the bandgap of ZnO. Typically, a two-step fast and slow rise and decay photocurrent behavior is observed for ZnO; however, there is still much debate concerning the predominant underlying physical processes used to describe these photocurrent behaviors that have been well documented in previous literature [4, 21, 32, 35, 36, 38, 43–49]. Furthermore, the literature remains a tangled web of information regarding these photocurrent behaviors. Therefore, we present the following review of NPDs, and photoconduction and recombination mechanisms in ZnO to elucidate the many photoconduction and recombination mechanisms which have been documented in literature, and to provide a foundation for understanding how NPD interactions with external atmospheric conditions, behavior as electron or hole traps, and sources of photocurrent generation can be used to describe the fast and slow rise and decay photoconductive behavior in our proposed physical models.

There are four main types of NPDs in ZnO: oxygen vacancies (V_o), zinc vacancies (V_{Zn}), zinc and oxygen interstitials (Zn_i, O_i), and antisites [23, 54]. Oxygen vacancies and zinc interstitials create donor levels, and the zinc vacancy is an acceptor level [23, 55]. Oxygen and zinc vacancies are considered to be the most predominant defects in ZnO [23, 56]. Theoretical studies have shown that the oxygen vacancy is actually a deep double donor, contrary to the notion that it created an abundant free-electron density and was responsible for the dominant n-type conductivity observed for ZnO [57]. Photoluminescence, electroluminescence, and density functional theory studies have shown that the neutral oxygen vacancy (V_o^0) lies ∼0.9–1.65 eV above the valence band (VB) edge [30, 58, 59],

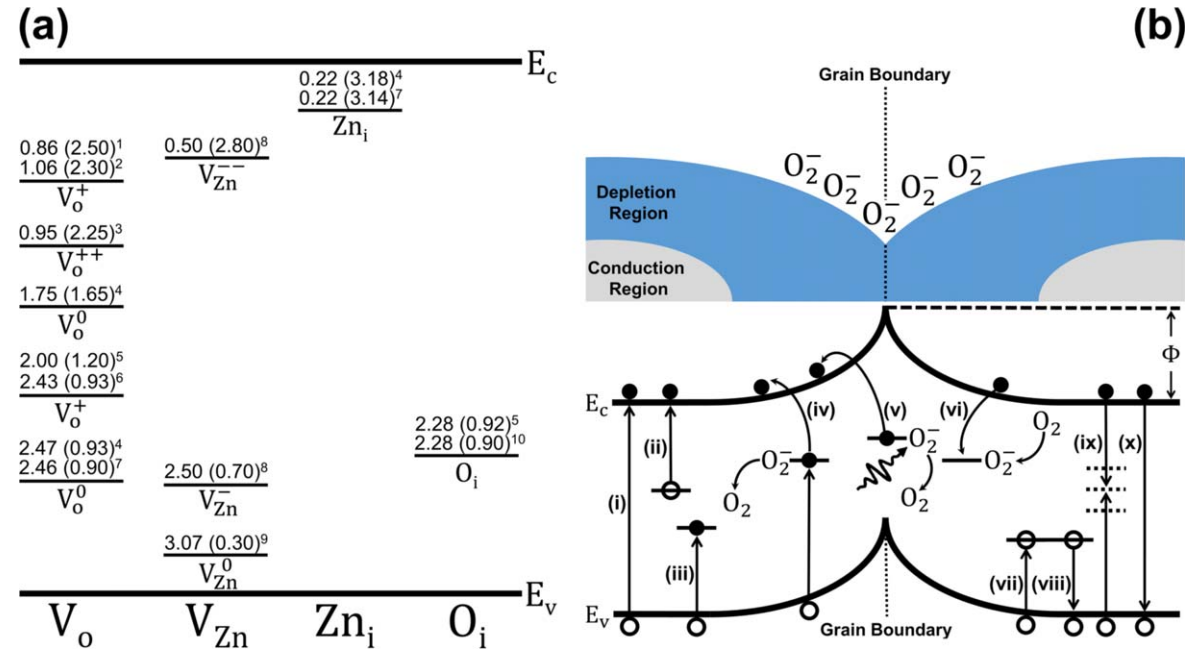

Figure 1. (a) The reported energy levels of various NPDs in ZnO: (1) [25], (2) [26], (3) [23], (4) [59], (5) [27], (6) [4], (7) [28], (8) [29], (9) [60], (10) [61]. (b) A schematic representation of two adjacent ZnO crystals showing the conduction and depletion regions, and the high density of adsorbed oxygen near the grain boundary. Below is the matching band diagram showing the photoconduction and recombination mechanisms in polycrystalline ZnO: electron–hole pair generation via (i) band-to-band, (ii) defect level to conduction band, and (iii) valence band to defect level. Oxygen desorption via (iv) hole capture, and (v) a photon-assisted molecule desorption mechanism. (vi) Oxygen adsorption. Hole (vii) capture and (viii) release to and from a defect state. Electron–hole recombination (ix) at a recombination center and (x) via band-to-band recombination.

while its singly (V_o^+) and doubly (V_o^{++}) charged oxidation states have been reported to lie ∼0.9–2.5 eV [4, 25–27] and ∼2.25 eV [23] above the VB edge, respectively. The zinc vacancy has three possible charge states: V_{Zn}^0, V_{Zn}^-, and V_{Zn}^{--} [31, 55], which are reported to lie ∼0.3 eV [60], ∼0.7 eV [29], and ∼2.8 eV [29] above the VB edge, respectively. The zinc interstitial is a shallow double donor which lies ∼3.18 eV (∼0.22 eV) above the VB (below the conduction band (CB)) [28, 59], and the oxygen interstitial has been reported to lie ∼0.9 eV above the VB [27, 61]. The reported energy levels for a variety of NPDs in ZnO are shown in figure 1(a). The distances in eV from the CB (VB) are shown above their respective NPD type as reported from literature. The wide range in reported values of the various NPD energy levels is due, in part, to the complexity of the analyzation of photoluminescence spectra arising from the numerous acceptor–donor combinations that can match experimental photoluminescence energies, and is exacerbated by the variations of the theoretically calculated defect energy levels as shown in figure 1(a) and in the band diagram included in an article by Tam *et al* [62].

It is well known that in the dark, free electrons from ZnO are captured by the adsorption of oxygen on the ZnO surface, which induces an upward band bending, forming a low conductivity depletion region on the surface of a NW [35, 36, 43, 45–47]. In the case of polycrystalline ZnO, a depletion region is formed at the grain boundary between two adjacent crystals. Grain boundaries of polycrystalline ZnO have been shown to contain a higher density of defects compared to grain centers, and grain boundaries host the numerous defect sites that are responsible for the adsorption of oxygen molecules [32]. According to density functional theory, a dissociative chemisorption of atmospheric oxygen occurs at the oxygen vacancy defect site of ZnO by filling the vacant oxygen site with one atomic oxygen [63]. Physisorption was also found to occur on the surface of defect-free ZnO, however, because of the abundance of oxygen vacancies in ZnO, oxygen vacancy defect sites were found to be the more favored adsorption sites for oxygen [63]. These results suggest that chemisorption is preferred over physisorption, and that chemisorption of atmospheric oxygen occurs at oxygen vacancy defect sites that are abundant on the structurally disordered grain boundaries of polycrystalline ZnO.

Figure 1(b) is a schematic representation showing two adjacent ZnO nanocrystals displaying the grain boundary, with a corresponding band diagram and upward band bending induced by the adsorption of atmospheric oxygen to the high density of oxygen vacancy defect sites on the structurally disordered grain boundary. The potential barrier formed by the adsorption of atmospheric oxygen on the grain boundary gives rise to a conduction and depletion region allowing for the separation of electrons and/or holes during illumination with UV and sub-bandgap excitation sources. Typically, the initial rapid rise in ZnO photocurrent is attributed to band-to-band excitations of electron–hole pairs in the case of UV excitation [3, 45, 64], and to excitations of electron–hole pairs arising from optical transitions between defect states and the CB in the case of sub-bandgap illumination [21, 23, 65]. In the former case, holes are swept to the grain boundary via the built-in potential; in the latter, holes are trapped in defect

levels lying within the bandgap. In both cases, the separation of photogenerated holes and electrons increases the electron lifetime, as they are unlikely to recombine with holes. The result is a rapid increase in photocurrent. Sub-bandgap illumination can also excite electrons from the VB to a defect level lying within the bandgap [23, 32]. Here, holes are created in the VB, and the excited electrons that are confined to the defect level do not significantly contribute to the total conductivity. In this case, an increase in conductivity is attributed to a mechanism by which holes swept to the surface via the potential gradient release adsorbed oxygen through an electron–hole recombination mechanism to remove oxygen from the surface (oxygen desorption), thereby releasing trapped electrons which are then able to contribute to the conductivity [32]. These three electron–hole pair generation mechanisms for UV and sub-bandgap excitation are shown in figure 1(b) and labeled as processes (i)–(iii). The oxygen desorption mechanism is labeled as process (iv) in figure 1(b). A significant photocurrent response is also suggested to occur via a photon-assisted molecule desorption (PAMD) mechanism, where surface adsorbed oxygen is desorbed via sub-bandgap excitation on the surface of ZnO NWs [35, 36] and V_2O_5 NWs [66]. It is well known that the activation energy for the desorption of chemically adsorbed oxygen from ZnO is ∼1.0 eV [67]. In the PAMD mechanism, oxygen is desorbed from the surface via an excitation energy greater than the activation energy for oxygen desorption, thereby releasing trapped electrons into the CB. The PAMD mechanism is labeled as process (v) in figure 1(b). In all the aforementioned photocurrent generation mechanisms, the accumulation of holes on the grain boundary and the removal of oxygen from the surface reduce the barrier height, which further increases conductivity and contributes to the observed initial fast rise in photocurrent.

Following the rapid rise is a slow rise in photocurrent which has been attributed to the competition between the oxygen-related adsorption and desorption mechanisms [36, 46, 47]. Oxygen can be desorbed via the hole-release mechanism and/or the PAMD mechanism. In both desorption mechanisms, trapped electrons are released, contributing to the conductivity. Competing with the oxygen desorption processes is the adsorption of oxygen that traps electrons from the CB and the recombination of electrons and holes at recombination centers, where both processes decrease the conductivity. Ultimately, the combination of these processes results in a slow increase in photocurrent that eventually saturates when the generation and recombination rates reach a steady state. The rate of the slow rise in photocurrent is affected by the concentration of atmospheric oxygen [35, 36, 47, 68], further suggesting that the slow photocurrent rise response is dominated by the competition between the oxygen related adsorption and desorption mechanisms.

The initial rapid decay of photocurrent following termination of illumination has been attributed to the recombination of electrons and holes via band-to-band recombination [21, 43, 44], and via trap-assisted (Shockley–Read–Hall) recombination [21, 69]. The radiative portion of these recombination processes can be examined with photoluminescence spectra and time-resolved photoluminescence transients that occur on the order of ∼ns following termination of illumination [21]. The initial rapid decay of the photocurrent has also been attributed to a process by which photo-desorbed oxygen in the bulk of polycrystalline ZnO is quickly re-chemisorbed after termination of the illumination source [42]. In this case, the majority of the chemisorbed oxygen is assumed to be in the bulk of the material, where it is not able to be heavily influenced by external oxygen concentrations [42]. The low barrier height at the termination of illumination also facilitates the re-adsorption of oxygen on the surface where electrons in the CB can more easily overcome a relatively low energy barrier, resulting in a quick reduction of the photocurrent.

There are two primary models that have been used to describe the slow photocurrent decay process, which can exhibit a long decay on the order of hours or days and is typically referred to as a persistent photoconductivity [21, 33–36, 38, 40, 45–48, 70–73]. The first model attributes the slow portion of the photocurrent decay to the competition between the oxygen adsorption and desorption mechanisms [35, 45, 47, 68]. The other model attributes this slow decay to a process by which oxygen vacancies are excited to a metastable state following a lattice relaxation where the recapture of electrons in the metastable state is prohibited via a thermally activated barrier [74]. In the former case involving the competition between the oxygen adsorption and desorption mechanisms, band bending at the grain boundary is increased as oxygen is re-adsorbed on the surface, which decreases the probability for an electron to overcome the increased energy barrier. Simultaneously, holes swept to the grain boundary via the potential gradient release adsorbed oxygen on the surface, freeing electrons that then contribute to the conductivity. The competition of the oxygen adsorption and desorption mechanisms results in the slow decrease in the photocurrent. The rate of decay for the slow portion of the photocurrent has been shown to be highly dependent on atmospheric conditions, namely oxygen concentration, suggesting that the surface-related oxygen adsorption and desorption mechanisms are the dominant processes responsible for the slow photocurrent decay [35, 36, 46, 47, 68, 71]. The effects of the slow surface-related oxygen adsorption and desorption mechanisms on the photocurrent decay are also confirmed with studies of photocurrent decay of ZnO with passivated samples [21, 45, 75]. Here, the surface passivation of ZnO inhibits the oxygen-related adsorption and desorption mechanisms, leading to an increased rate of photocurrent relaxation. An additional mechanism giving rise to the slow decay of photocurrent involves the trapping and subsequent emission of electrons and/or holes to and from deep defect levels within the bandgap [21]. A NPD behaving as a hole trap repels electrons and has a small electron capture cross section resulting from a negative charge when the hole trap is filled with a hole [21]. Therefore, in contrast to recombination centers, NPDs exhibit slow electron–hole recombination because holes are typically thermally emitted into the VB before recombination with an electron to desorb oxygen, recombination at a recombination center, or re-trapped in

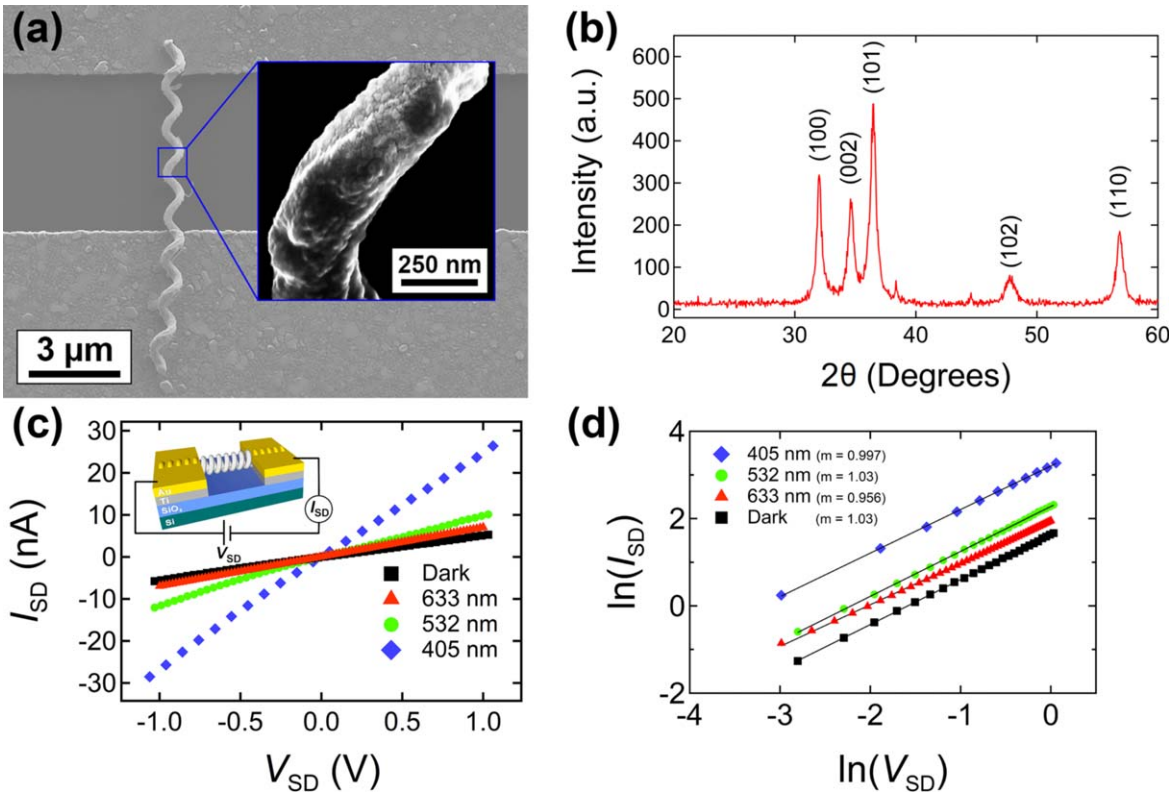

Figure 2. (a) SEM images of the single ZnO-NS device and inset showing the surface morphology of the polycrystalline ZnO coating. (b) Powder XRD 2θ pattern of ZnO-NSs. (c) Source-drain current–voltage curves of the ZnO-NS device in the dark and when illuminated with 405, 532, and 633 nm excitation sources. The inset shows a 3D representation of the device with an electrical diagram. (d) A ln–ln plot showing the Ohmic behavior of the source-drain current–voltage curves.

another NPD hole trap. These hole trapping and photocurrent generation and recombination mechanisms, and how they affect the photocurrent rise and decay will be further discussed in detail in the following sections, which present physical models to describe the near-UV and sub-bandgap photocurrent rise and decay responses observed in our experiments.

4. Single ZnO-NS device and ZnO structure

Figure 2(a) shows SEM images of the single ZnO-NS device that was used in our experiments. The single ZnO-NS spans a $\sim$5 μm long gap between two Ti/Au electrical contacts forming the source-drain electrodes. The inset in figure 2(a) is an SEM image of the ZnO-NS surface and shows the uniformly distributed polycrystalline ZnO coating which has an average particle size of $\sim$20 nm. The ZnO ALD process used to coat the NS produces a uniform $\sim$70 nm thick ZnO layer on the surface of the silica NS [10, 53] and has been demonstrated to be advantageous over other deposition methods, such as CVD, as it allows the user to control the thickness of the coating, the size of the ZnO nanocrystals, and the ability to coat intricate three-dimensional (3D) shapes [9, 11]. Control of the ZnO nanocrystalline size is particularly important in the application of ZnO-NSs used as redox chemical sensors where the ZnO nanocrystalline size was shown to be a significant factor in the response of the sensors when exposed to explosive compounds [11]. The platform for the ZnO coating is a non-conducting silica NS. The helical silica NS structure serving as a platform for the ZnO is particularly interesting because of its high surface area compared to a NW of similar dimensions. For example, the silica NS with a $\sim$70 nm thick coating of ZnO and 5 μm free length as shown in figure 2(a) has $\sim$5 times more surface area than a 70 nm diameter, 5 μm long ZnO NW.

The crystalline structure of the ZnO coating was characterized with XRD. Figure 2(b) shows the powder XRD pattern of an ensemble of nanocrystalline ZnO-NS structures collected in the 2θ range of 20°–60°. The diffraction peaks observed at $2\theta = 32.02$, 34.55, 36.50, 47.81, and 56.87 correspond to lattice planes (100), (002), (101), (102), and (110), respectively, indicating the polycrystalline hexagonal Wurtzite structure of the ZnO [53].

5. Photoconductivity

5.1. Voltage dependence of the photocurrent and ZnO resistivity

Figure 2(c) shows the source-drain current–voltage (I_{SD}–V_{SD}) characteristics of the single ZnO-NS device under dark conditions and when illuminated with 405, 532, and 633 nm excitation sources. The inset in figure 2(c) shows a 3D

representation of the device with an electrical diagram. The excitation intensity measured at the sample was 2 mW cm^{-2} for each illuminated I_{SD}–V_{SD} measurement. Figure 2(d) shows a ln–ln plot of the dark and illuminated I_{SD}–V_{SD} characteristics which exhibit an Ohmic response (unity slope), suggesting that there is unimpeded transfer of the majority carriers (electrons) between the Ti/Au-ZnO interface.

The total resistance (R_T) of the single ZnO-NS device is the sum of the resistance of the ZnO-NS ($R_{ZnO\text{-}NS}$) and of the two contact resistances attributed to the Ti-Au/ZnO-NS contacts on each end of the device ($2R_C$): $R_T = R_{ZnO\text{-}NS} + 2R_C$. The specific contact resistance of Ti/Au contacts to ZnO has been studied extensively and reported to be in the range of $\sim 10^{-3}$ to 10^{-8} Ω cm^2 [76–79]. The estimated contact resistance of our device is small (~20 kΩ), ~4 orders of magnitude lower than the total resistance of the device (~200 MΩ), and therefore can be neglected. The resistivity, ρ, of the device was calculated using

$$\rho = R_{ZnO\text{-}NS}\frac{A}{L}, \quad (1)$$

where A is the cross sectional area of the ZnO coating on the NS, and L is the length of the ZnO-NS. The cross sectional area of the ZnO layer was calculated by measuring the wire diameter of the ZnO-NS via an SEM image and using an estimation of the ZnO thickness (~70 nm) based on previous measurements of the thickness of a ZnO coating deposited on a Si substrate under similar ALD conditions [10, 53]. The helical pitch of individual NSs are random and varied during the growth process; however, are usually well-defined for micron-long sections of its free length. The well-defined and constant helical pitch of the NS across the electrode gap was exploited to calculate the length, L, of the ZnO-NS device. The resistivity of the single ZnO-NS in the dark was 166 Ω cm, and is in agreement with previous measurements of the resistivity of thin-film ZnO (~1–1000 Ω cm) [80, 81]. The illuminated resistivities for $\lambda = (405, 532, 633)$ nm were $\rho = (34, 83, 125)$ Ω cm. The largest change in conductance occurs under illumination with the 405 nm excitation source, which is increased by a factor of ~5 compared to the dark conductance.

5.2. Near-UV and sub-bandgap photocurrent rise and decay response

Figure 3 shows the normalized photocurrent response of the single ZnO-NS device when illuminated with near-UV (405 nm) and sub-bandgap (532 and 633 nm) excitation sources. The inset in figure 3 shows the details of the on/off behavior for the 532 and 633 nm excitation sources. The photocurrent (I_{pc}) was determined by subtracting the dark current (I_d) from the total illuminated current, and we define the normalized photocurrent as the ratio of the photocurrent to the dark current (I_{pc}/I_d). The shaded area represents the 15 min period when the device was illuminated with the respective excitation source. The applied bias was +0.5 V and the intensity of the excitation source was 2 mW cm^{-2} for each photocurrent response measurement. The single ZnO-NS device was held at a +0.5 V applied bias for ~2 h in the dark to achieve a steady state dark current prior to illumination with each respective excitation source. The photocurrent responses of each excitation source display a typical two-step fast and slow rise and decay behavior. First, there is an initial fast increase followed by a slow increase in photocurrent which takes minutes to hours to saturate; when the illumination source is terminated there is an initial fast decrease followed by a slow decrease in photocurrent which takes hours to return to its initial steady state dark current value.

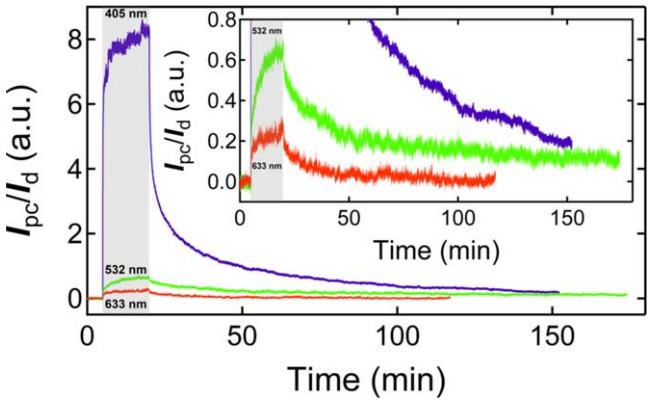

Figure 3. The normalized photocurrent response of the single ZnO-NS device when illuminated with 405, 532, and 633 nm excitation sources and inset showing the details of the on/off behavior for the 532 and 633 nm excitation sources. The shaded area represents the 15 min period when the device was illuminated with the respective excitation source.

5.3. Near-UV and sub-bandgap photocurrent rise response

Figure 4 shows the details of the fast and slow normalized photocurrent rise response of each excitation source and the corresponding fits and time constants attained with a double exponential function that was used to separately analyze and compare the two-step photocurrent rise response of each excitation source. The shaded area represents the 15 min period when the device was illuminated with the respective excitation source. The normalized photocurrent growth for all three wavelengths was fitted with a double exponential equation of the following form:

$$I_n(t) = A_0 - B_1 e^{-\frac{t-t_0}{\tau_1}} - B_2 e^{-\frac{t-t_0}{\tau_2}}, \quad (2)$$

where I_n is the normalized photocurrent (I_{pc}/I_d), A_0, B_1, and B_2 are positive constants, t_0 is the time when the illumination source was turned on, and τ_1 and τ_2 are the fast and slow time constants, respectively. The time constants attained from the double exponential fits are $\tau_1 = (4.8, 5.5, 12)$ s and $\tau_2 = (300, 251, 2550)$ s for $\lambda = (405, 532, 633)$ nm.

There is a strong response to the 405 nm (3.06 eV) near-UV excitation source and the photocurrent increases from I_d by a factor of ~6 in 10 s then slowly increases by an additional factor of ~2 after 15 min. The observed sub-bandgap photocurrent response for the 532 and 633 nm excitation sources suggests that there are an abundance of NPDs in the polycrystalline ZnO [32]. It is well known that the bandgap of bulk defect-free ZnO is 3.37 eV; however, a reduction in the

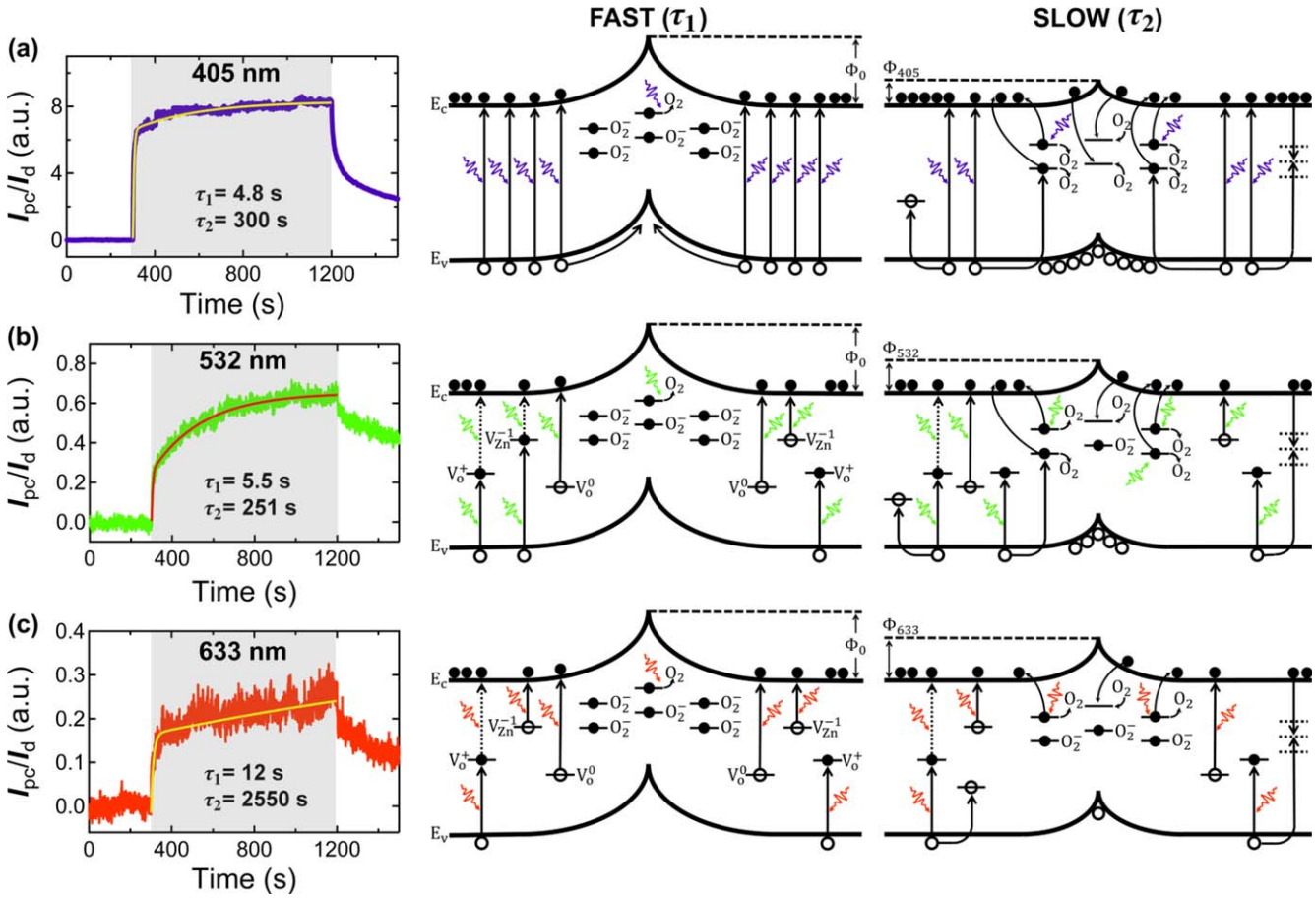

Figure 4. The normalized photocurrent rise characteristics of the (a) 405 nm, (b) 532 nm, and (c) 633 nm excitation sources showing double exponential fits and corresponding time constants for photocurrent growth. The shaded areas represent the 15 min period when the device was illuminated with the respective source. Displayed to the right of each photocurrent rise response are the corresponding band diagrams which show the dominant photocurrent generation and recombination mechanisms for the fast and slow photocurrent rise response of each respective excitation source.

bandgap can be achieved with the introduction of oxygen vacancies [82]. Calculations of the density of states for ZnO with an ideal defect-free Wurtzite structure and for a Wurtzite structure containing 6.25% oxygen vacancies have shown that the bandgaps of these two structures are 3.22 eV and 2.91 eV [82], respectively, and lower than that of bulk defect-free ZnO. The 405 nm photocurrent response is ∼13× greater than the photocurrent response of the 532 nm excitation source and ∼30× greater than the photocurrent response of the 633 nm excitation source 15 min after illumination. The strong photocurrent response of the 405 nm source cannot be attributed solely to excitations occurring between defect states and the CB. In our photoconductivity measurements, the number of excited carriers is proportional to the excitation energy of the respective source using a constant illumination intensity (2 mW cm^{-2}); therefore, we would expect a proportional increase in the saturation current for the 405, 532, and 633 nm excitation sources if they are exciting transitions from similar defect levels. We observe this proportional increase with the 532 and 633 nm excitation sources, but not with the 405 nm excitation source. A similar proportional increase in photocurrent was observed by Lee *et al*, who observed a proportional increase of the photocurrent response of ZnO to red, green, and blue illumination sources, and a large disproportionate photocurrent response to UV [83]. Additionally, the non-negligible spectral bandwidth of the 405 nm excitation source may allow for band-to-band transitions greater than 3.06 eV. We therefore attribute the dominant mechanism for the initial strong and rapid response of the photocurrent for the 405 nm excitation source to band-to-band excitations of electron–hole pairs, which is consistent with a reduction of the bandgap from the confirmed Wurtzite structure and presence of defects in the material, and the non-negligible spectral bandwidth of the 405 nm excitation source. During the fast photocurrent response, the initial band bending present before illumination quickly separates photogenerated electrons and holes with electrons confined to the conduction region and holes swept to the grain boundary, increasing the electron lifetime and resulting in the observed quick increase in the photocurrent. The PAMD mechanism also removes adsorbed oxygen from the surface and lowers the potential barrier. The slow rise in photocurrent can be understood in terms of the surface-related oxygen adsorption and desorption mechanisms. Oxygen desorption occurs due to the PAMD mechanism and the hole-assisted recombination mechanism with adsorbed oxygen. The large accumulation of

holes on the grain boundary and the oxygen desorption mechanisms lower the potential barrier and increase the probability for electrons in the conduction region to overcome the barrier and re-adsorb oxygen on the surface. The competition between the surface-related oxygen desorption mechanisms and the oxygen adsorption mechanism results in a slow increase in the current that saturates when the rates of these two processes reach a steady state.

The photocurrent for the 532 nm (2.33 eV) excitation source initially increases from I_d by ~20% in 10 s, then slowly increases by an additional ~45% after 15 min. In this case, the fast response can be attributed to the generation of electron–hole pairs due to optical transitions between the VB and intermediate defect levels, and between intermediate defect levels and the CB. Possible transitions from the VB to intermediate defect levels include VB $\rightarrow V_o^+$ [32] and VB $\rightarrow V_{Zn}^{-1}$ [23], and possible transitions from intermediate defect levels to the CB include $V_{Zn}^{-1} \rightarrow$ CB [23, 65] and $V_o^0 \rightarrow$ CB [74]. A second transition from an excited state in the intermediate defect level to the CB is possible if the energy level of the excited state lies less than 2.33 eV below the CB edge [23]. Significant hole trapping occurs due to transitions from intermediate defect levels to the CB, and fewer holes are swept to the grain boundary as compared to the 405 nm excitation source. The holes that form a bound exciton with an electron excited from an intermediate defect level into the CB are likely to be deeply trapped and unable to thermally relax back to the VB, while holes trapped closer to the VB thermalize back to the VB to then be re-trapped, recombine with a trapped electron on the surface to desorb oxygen, or recombine with an electron at a recombination center. Additionally, holes created due to excitation from intermediate defect states to the CB may become deeply trapped as a result of the subsequent distortion of the surrounding lattice [84]. For example, Penfold *et al* have shown using simulations and x-ray absorption spectroscopy combined with a dispersive x-ray emission spectrometer, that photoexcited holes in ZnO nanoparticles become trapped at V_o^+ sites where, after the outward displacement of the surrounding zinc atoms, becomes a V_o^{++} site [84]. Significant hole trapping results in a reduced oxygen desorption rate relative to that with the 405 nm excitation source, resulting in a slow rise of the photocurrent. Note that the initial barrier height should be the same for all three excitation sources, as the device was held in the dark for ~2 h to achieve a steady state dark current prior to illumination. We postulate that the dominant process which acts to desorb surface oxygen and reduce the barrier height for the 532 nm excitation source is due to the PAMD mechanism. The change in the height of the barrier for the 532 nm excitation source is much less than with the 405 nm excitation source as a consequence of greater hole trapping, which results in fewer surface oxygen being desorbed. The higher barrier height with 532 nm, as compared to the 405 nm excitation source, in conjunction with significant hole trapping, increases the rate of rise for the slow portion of the 532 nm photocurrent rise response, as the two effects lower the probability for electrons to overcome the barrier and adsorb surface oxygen.

The photocurrent for the 633 nm (1.96 eV) excitation source initially increases from I_d by ~10% in 10 s and then very slowly increases by an additional ~15% after 15 min. Similar to the 532 nm excitation source, the fast rise response is attributed to the generation of electron–hole pairs due to optical transitions between the VB and intermediate defect levels, and between intermediate defect levels and the CB. A possible transition from the VB to an intermediate defect level is VB $\rightarrow V_o^+$ [32] for V_o^+ lying less than 1.96 eV above the VB edge, and possible transitions from intermediate defect levels to the CB include $V_{Zn}^{-1} \rightarrow$ CB [23, 65] and $V_o^0 \rightarrow$ CB [74]. The broad range of reported energy levels as displayed in figure 1(a) makes it difficult to determine if the VB $\rightarrow V_o^+$ transition is possible for the 633 nm excitation source. If the V_o^+ level lies more than 1.96 eV above the VB edge, the VB $\rightarrow V_o^+$ transition is not possible. A second transition from V_o^+ to the CB is possible if the energy level is less than 1.96 eV below the CB or if, after a lattice distortion, the energy level changes and allows the transition [23, 84]. Nevertheless, we postulate that the majority of the transitions occur from intermediate defect states to the CB, resulting in the vast majority of holes created during illumination being trapped in deep intermediate defect states and unable to desorb surface oxygen at a rate comparable to the 532 and 405 nm excitation sources. This results in the smallest change in the potential barrier height, as compared to the 532 and 405 nm excitation sources. The slow photocurrent rise time constant is the greatest of all three excitation sources ($\tau_2 = 2550$ s). We attribute the very slow photocurrent rise characteristics to a combination of the PAMD mechanism and the aforementioned hole trapping resulting from photoexcitation of carriers from intermediate defect states to the CB. Here, oxygen is desorbed via the PAMD mechanism; however, the high potential barrier and trapped holes means that oxygen cannot be sufficiently re-adsorbed at a rate comparable to the 405 and 532 nm excitation sources. The result is a slow rise in the photocurrent that does not saturate and an abundance of oxygen left on the surface, as compared to the 405 and 532 nm excitation sources, which is attributed to significant hole trapping. Similar very slow photocurrent rise characteristics have been observed for a single ZnO NW device under vacuum, where the re-adsorption of oxygen was inhibited, resulting in a slow photocurrent rise response due to the rate of oxygen desorption being faster than the rate of adsorption [47].

5.4. Near-UV and sub-bandgap photocurrent decay response

Displayed in figure 5 are the normalized fast and slow photocurrent decay responses for each excitation source and the corresponding fits and parameters attained with a Kohlrausch stretched exponential function. The insets are expanded views of the initial fast decay behavior of the device within the first 20 s after termination of illumination. The shaded areas represent the period when the device was illuminated with the respective source. The photocurrent decay curves are best fit

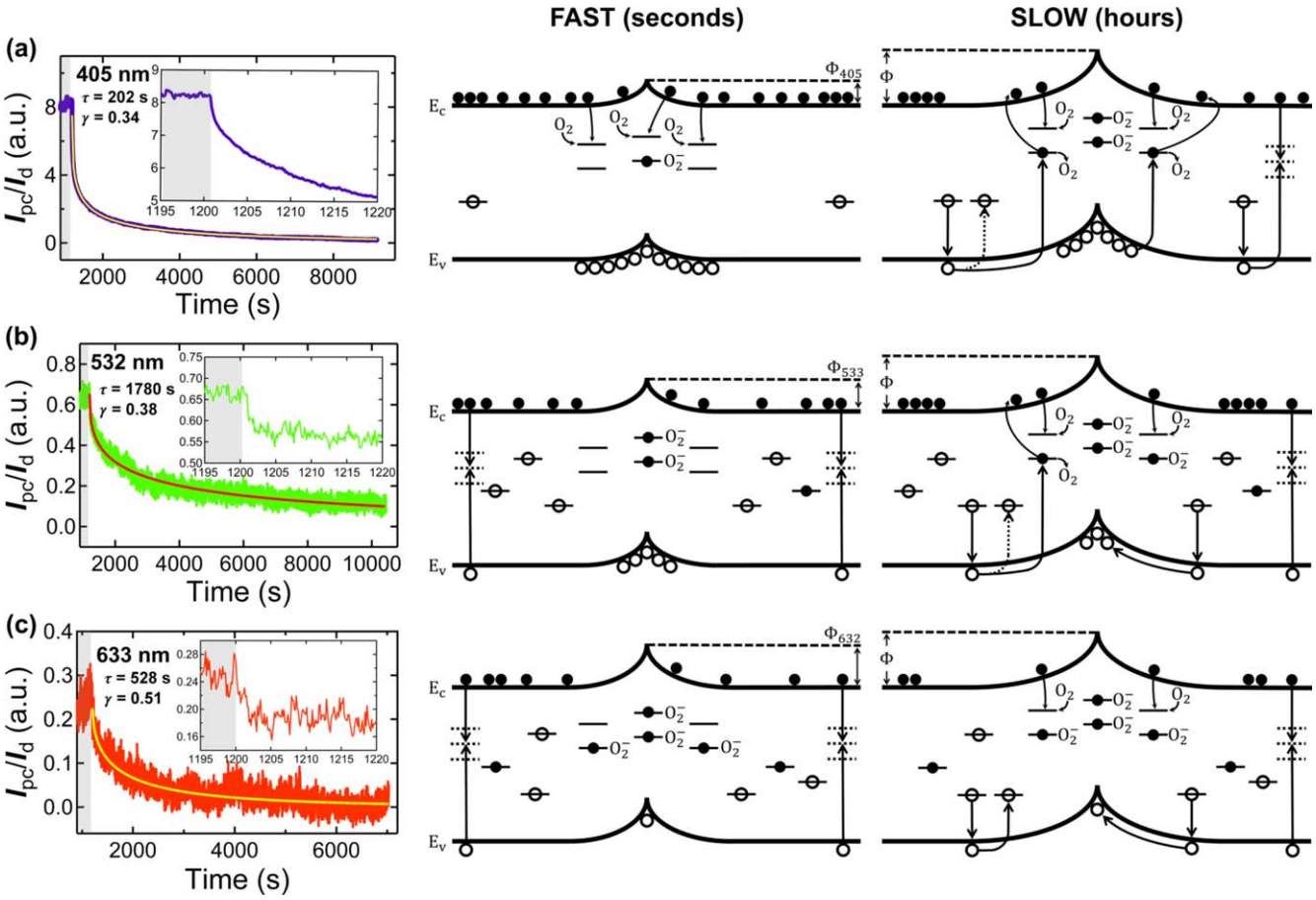

Figure 5. The normalized photocurrent decay characteristics of the (a) 405 nm, (b) 532 nm, and (c) 633 nm excitation sources, where the solid lines are fits obtained using the Kohlrausch stretched exponential function. The insets in each photocurrent decay plot show the initial fast decay behavior within the first 20 s after termination of illumination. The shaded areas represent the periods when the device was under illumination with the respective excitation source. Displayed to the right of each decay curve are the corresponding band diagrams showing the dominant photocurrent relaxation mechanisms for the fast and slow decay responses.

with a Kohlrausch stretched exponential function and a double exponential function, regardless of the excitation source. The Kohlrausch stretched exponential function is generally used to describe decay in systems that exhibit multiple energy transfer mechanisms [38, 40, 68, 70, 85] and is of the form

$$I_{\rm n}(t) = C{\rm e}^{-(t/\tau)^{\gamma}}, \tag{3}$$

where $I_{\rm n}$ is the normalized photocurrent ($I_{\rm pc}/I_{\rm d}$), C is a positive constant, τ is the relaxation time constant, and γ is a stretching parameter in the range $0 < \gamma \leqslant 1$. The Kohlrausch stretched exponential function becomes a classical single exponential function in the limit $\gamma \to 1$, at which point the differences in energy transfer mechanisms are indistinguishable [40]. The fitting parameters for the Kohlrausch stretched exponential function in figure 5 are $\tau = (202, 1780, 528)$ s and $\gamma = (0.34, 0.38, 0.51)$ for $\lambda = (405, 532, 633)$ nm. The Kohlrausch stretched exponential function is a convenient model to describe systems that deviate slightly from classical single exponential behavior; however, because there is such a large spread in reported values of γ and τ in the literature for ZnO photocurrent decay, it is difficult to distinguish and associate the parameters with an underlying physical process [38, 40, 68]. Therefore, we have also provided the parameters attained with a fit of a double exponential function. The double exponential function for the photocurrent decay has the form

$$I_{\rm n}(t) = D_0 + F_1{\rm e}^{-\frac{t-t_1}{\tau_3}} + F_2{\rm e}^{-\frac{t-t_1}{\tau_4}}, \tag{4}$$

where $I_{\rm n}$ is the normalized photocurrent ($I_{\rm pc}/I_{\rm d}$), D_0, F_1, and F_2 are constants, t_1 is the time at termination of illumination, and τ_3 and τ_4 are the fast and slow relaxation time constants, respectively. The time constants attained with the double-exponential fits are $\tau_3 = (107, 711, 425)$ s and $\tau_4 = (1676, 4655, 5571)$ s for $\lambda = (405, 532, 633)$ nm.

When the 405 nm excitation source is turned off, there is an initial sharp decay of the photocurrent that decreases by ∼19% of its value at termination of illumination ($I_{t_{\rm off}}$) within 2 s, followed by a slow decay that decreases by ∼97% of $I_{t_{\rm off}}$ after 2 h. As discussed earlier, the radiative portion of the recombination processes occurs on the order of ∼ns upon termination of illumination [21]. Therefore, the observed photocurrent decay and the corresponding recombination mechanisms on the order of seconds–hours are non-radiative recombination processes. The initial rapid decay of the photocurrent is likely due to the quick re-adsorption of oxygen at

grain boundaries or near the surface. The low potential barrier immediately following termination of illumination facilitates the re-adsorption of oxygen on the surface due to the high probability of an electron in the CB overcoming the low barrier to re-adsorb oxygen at grain boundaries or near the surface. Also, with 405 nm excitation there is much less hole trapping and more holes are accumulated on the grain boundary, as compared to the 532 and 633 nm excitation sources. This allows for a faster rate of the desorption of oxygen from the surface, keeping the potential barrier lower and allowing for a quicker recovery of the current during the fast decay process compared to the 532 and 633 nm excitation sources. As the oxygen adsorption and desorption processes continue, there is a gradual accumulation of negative charge at the surface that increases the band bending, and in turn slows the rate of photocurrent decay as the probability for an electron to overcome the potential barrier and re-adsorb oxygen decreases. Ultimately, it is then the competition between the surface-related oxygen desorption mechanism, recombination, and oxygen re-adsorption mechanism that are responsible for the slow decay of the current, which eventually saturates when the oxygen desorption and recombination rates reach a steady state.

With 532 nm illumination, there is a small, but notable, initial rapid decay of the photocurrent that decreases by ∼12% of $I_{t_{\text{off}}}$ within 2 s, as shown in the inset of figure 5(b). The initial rapid decay of the photocurrent can be attributed to trap-assisted recombination and/or the quick re-adsorption of oxygen at grain boundaries or near the surface. The high potential barrier immediately following the termination of illumination decreases the probability for electrons in the CB to overcome the barrier to quickly facilitate the re-adsorption of oxygen. Therefore, we attribute the initial rapid decay in the first 2 s to trap-assisted recombination of electrons and holes. The slow decay of the photocurrent with 532 nm illumination is the slowest of the illumination sources used in this study, where the photocurrent only decreases by ∼80% of $I_{t_{\text{off}}}$ after 2 h. We attribute this very slow decay of the photocurrent to the oxygen adsorption and desorption mechanisms, where the oxygen desorption mechanism is considerably hindered as a result of the significant hole trapping. Here, very few holes are swept to the grain boundaries because they are in deep traps. Alternatively, holes are thermally emitted back to the VB where they can desorb surface oxygen to free electrons, be re-trapped, or combine with an electron at a recombination center. The combination of deep hole trapping associated with sub-bandgap excitation and the corresponding high potential barrier leads to increased carrier lifetimes and an extreme persistence in the photocurrent.

Like the 532 nm decay response, the 633 nm decay response exhibits an initial rapid decay of the photocurrent that decreases by ∼25% of $I_{t_{\text{off}}}$ within 2 s and is attributed to trap-assisted recombination of electrons and holes. Unlike 405 and 532 nm illumination, the 633 nm photocurrent decays back to the dark current value and does so in only 1.5 h following termination of illumination, which is the quickest recovery of all the illumination sources. We postulate that immediately following termination of illumination, a very small number of holes diffuse to the grain boundary, as compared to the 405 and 532 nm excitation sources. This is attributed to holes trapped in deep defect levels associated with 633 nm illumination, which primarily excited electron–hole pairs from mid-gap defect levels to the CB. Significant hole trapping in deep defect levels results in the lowest rate of the desorption of surface oxygen following termination of illumination, as compared to 405 and 532 nm excitation. Finally, based on the low photocurrent with 633 nm excitation relative to 405 and 532 nm excitation, the density of carriers in the CB is accordingly less. The low density of carriers combined with fewer surface oxygen sites available to re-adsorb oxygen results in a quicker recovery of the photocurrent, as compared to 405 and 532 nm excitation, because there are only a small number of carriers that recombine at recombination centers or assist with the re-adsorption of oxygen at the very few surface oxygen sites available. Hence, the recovery of the dark current for the 633 nm excitation source is the fastest of all three illumination sources.

5.5. Trap depth

The depths of the traps can be estimated from the photocurrent decay curves. The Bube model for photocurrent decay is given by the relationship, $I = I_0 \exp(-Pt)$, where I is the current at any time t, I_0 is the current at the moment of termination of illumination, and P is the probability rate of an electron (hole) escaping from a trap [86]. Since the electrons (holes) have a Maxwellian distribution of thermal energies, the probability rate that an electron (hole) will escape from a trap with a depth of energy E at a temperature T is $P = s \exp(-E/kT)$, where k is the Boltzmann constant (1.381×10^{-23} J K^{-1}), T is the absolute temperature, and s is the attempt to escape frequency [87]. The attempt to escape frequency is the product of the frequency at which phonons attempt to remove electrons (holes) from traps and the probability of transition from the trap to the conduction (valence) band [39, 87]. The attempt to escape frequency for ZnO has been found to lie between $\sim 10^9$ and 10^{11} Hz at room temperature [21, 87]. Combining the two relations, the energy of the trap depth at any time t along the photocurrent decay curve can be expressed as

$$E = kT\left[\ln(s) - \ln\left(\frac{\ln(I_0/I)}{t}\right)\right]. \tag{5}$$

The trap depths calculated from the photocurrent decay curves for each respective excitation source at 1, 10, and 100 min after termination of illumination (t_{off}) are given in table 1. The trap depths are given as a range using the low and high values of the attempt to escape frequency and vary from ∼0.65 to 0.82 eV 1 min after t_{off} to ∼0.74–0.91 eV 100 min after t_{off}. The trap depths in the slow portion of the photocurrent decay curves closely match the peak of the calculated hole trap density spectrum of ZnO epilayers of ∼0.9 eV [21] and estimations of the depths of traps in the sub-bandgap photoconductive decay in polycrystalline ZnO [22]. Penfold *et al* have shown using simulations and x-ray absorption spectroscopy combined with a dispersive x-ray emission

Table 1. Calculated trap depths at 1, 10, and 100 min after t_{off} using equation (5) and data from the photocurrent decay curves for each excitation source.

Wavelength (nm)	Trap depth (eV) 1 min	Trap depth (eV) 10 min	Trap depth (eV) 100 min
405	0.65–0.77	0.70–0.82	0.74–0.86
532	0.70–0.82	0.74–0.86	0.78–0.90
633	0.70–0.82	0.75–0.87	0.79–0.91

spectrometer that photoexcited holes in ZnO nanoparticles are trapped at V_o^+ defect sites that subsequently become V_o^{++} defect sites following an outward displacement of the surrounding zinc atoms [84]. The V_o^+ defect site has also been proposed as a source of hole trapping based on photoluminescence spectra and illumination of ZnO nanorods with a variety of sub-bandgap excitation sources [27]. The calculated trap depths for the slow portion of the photocurrent decay curves match the depth of the V_o^+ defect site lying ~0.93 eV above the VB edge [4] and are close to the estimated energy level of the V_o^{++} defect site lying ~1.18 eV above the VB edge [4].

5.6. Saturation photocurrent dependence on excitation intensity

The excitation intensity dependence of the saturation photocurrent (I_{sat}) on a ln–ln scale for the 405, 532, and 633 nm excitation sources is displayed in figure 6. The data was acquired in the range of ~0.1–2.0 mW cm^{-2} for all three excitation sources, where the applied bias was held at a constant +0.5 V. The ln–ln plots of the saturation photocurrent versus excitation intensity for all three wavelengths consist of distinct linear regions that follow a power law of the form, $I_{sat} = CI^{\alpha}$, where C is a constant, I is the intensity of illumination, and α is an exponent that defines the photocurrent response to excitation intensity. For 405 nm, three linear regions are observed with corresponding exponents of 0.56, 0.38, and 0.15. Only two linear regions are observed with the 532 and 633 nm excitation sources. With all illumination sources, the value of α decreases for successive linear regions and with increasing excitation intensity. The values of the exponents for the 532 and 633 nm excitation sources are $\alpha = (0.80,\ 0.22)$ and $\alpha = (1.1,\ 0.49)$, respectively. Values of $\alpha < 1$, i.e. sublinear dependence of the photocurrent on excitation intensity, correspond to trapping, recombination, and electron–hole pair generation within ZnO [88]. The sublinear dependence indicates a continuous and exponential distribution of electron traps between the CB and the electron Fermi level [39, 88, 89]. According to a physical model proposed by Rose [88] to describe the sublinear dependence of the photocurrent on excitation intensity, increasing the excitation intensity converts increasingly more of the electron trapping states to recombination states. The slow increase of the density of recombination states decreases the electron lifetime, resulting in the slow increase in the rise of the saturation photocurrent and observed sub-linearity [88].

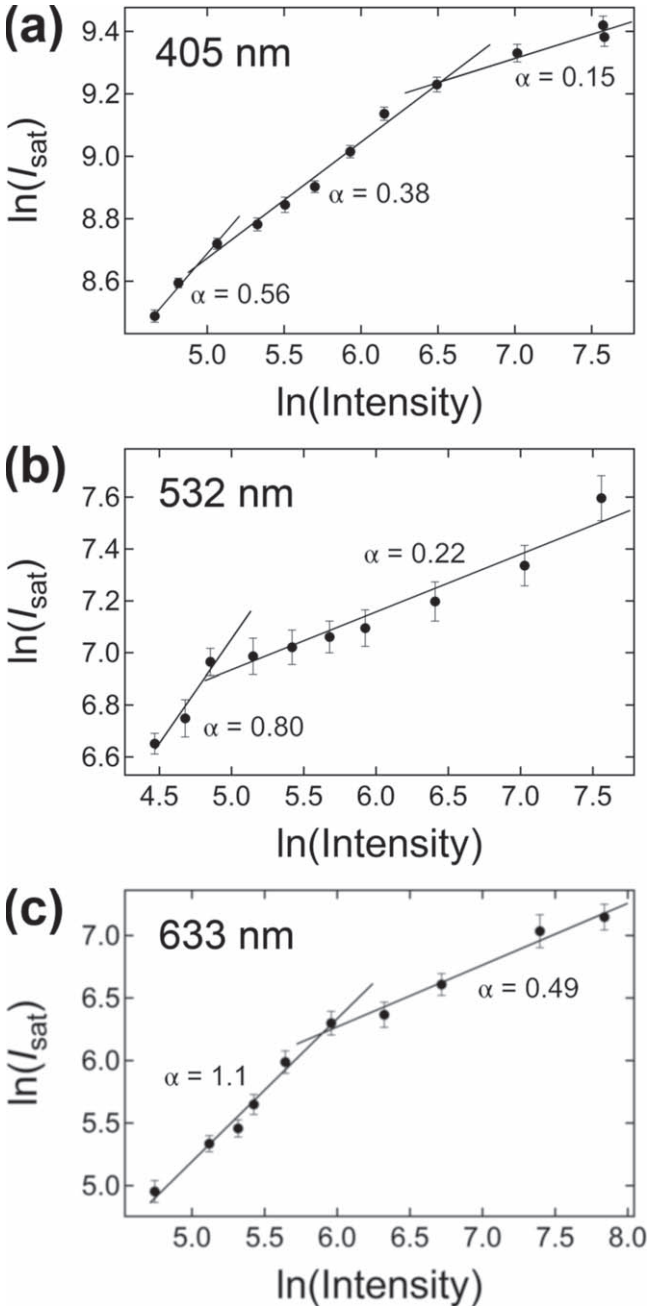

Figure 6. Saturation photocurrent as a function of excitation intensity on a ln–ln scale for (a) 405 nm (b) 532 nm and (c) 633 nm excitation sources. The applied bias was held constant at +0.5 V for each set of measurements.

Our results are in agreement with similar studies of ZnO NWs which also exhibit a sublinear dependence of the photocurrent on excitation intensity [1, 19, 33].

The responsivity of the single ZnO-NS device was calculated for each wavelength and at an excitation intensity of 0.1 mW cm^{-2}. The responsivity, R, is defined as the saturation photocurrent per unit of incident optical power and can be expressed as $R = I_{sat}/(IA)$, where I is the intensity of illumination and A is the irradiated area of the device. The responsivity was $R = (1740,\ 300,\ 28.9)$ A W^{-1} for $\lambda = (405,\ 532,\ 633)$ nm, and is on the order of the measured

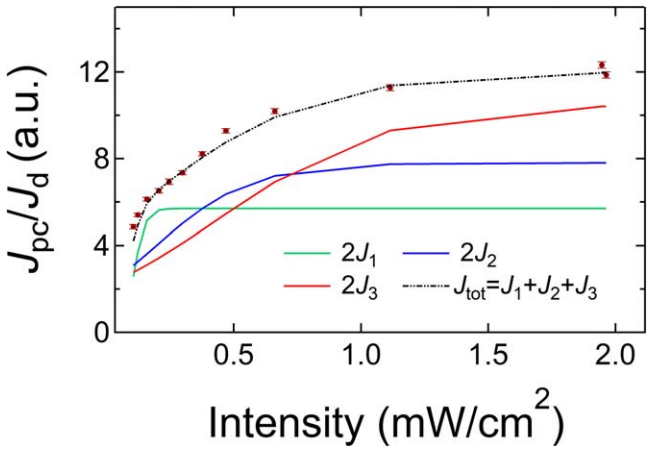

Figure 7. The normalized saturation photocurrent density versus excitation intensity profile of the single ZnO-NS device when illuminated with the 405 nm excitation source and fitted with a function given by equation (8). In the figure, the values of J_1, J_2, and J_3 are doubled to magnify the profile of each curve. Each curve shows a distinct rise and plateau that we attribute to different transition levels and rate of recombination processes.

responsivity of ZnO-based photodetectors comprised of surface functionalized ZnO NWs [17] and ZnO nanoparticles [41].

We propose a simple model to explain the break in the slope of the saturation photocurrent versus excitation intensity profile observed in figures 6 and 7. Figure 7 shows the normalized saturation photocurrent density versus excitation intensity profile for the 405 nm excitation source. The photocurrent density (J_{pc}) was determined by subtracting the dark current density (J_d) from the total illuminated current density, and we define the normalized saturation photocurrent density (J_{sat}) as the ratio of the photocurrent density to the dark current density (J_{pc}/J_d). We noted earlier that in the case of illumination with the 405 nm excitation source, the dominant photoconductive mechanism is the generation of band-to-band electron–hole pairs; however, photocurrent can be generated via multiple photoconductive mechanisms, including band-to-band electron–hole pair generation, a PAMD mechanism, and excitation of electron–hole pairs from the VB to intermediate defect states and from intermediate defect states to the CB. Recalling that the saturation photocurrent is taken as the photocurrent when the generation and recombination processes reach a steady state, as the intensity of the excitation source is increased the number of photons exciting electrons in the bandgap also increases, resulting in a higher saturation photocurrent. However, the rate of increase of the saturation photocurrent changes and tends to decrease, as shown in figure 7. Competing against the photogeneration of electron–hole pairs are processes that limit the total density of excited states and subsequently impede conduction, including the recombination of electron–hole pairs via direct recombination or at recombination centers, which becomes more significant as the intensity increases. As noted earlier, the rate of change of the saturation photocurrent with excitation intensity is due to the recombination rate arising from the increase in electron trapping states becoming recombination states as the excitation intensity is increased [39, 88]. In line with this, it is understood that the rate of recombination increases as more electrons and holes are generated. Furthermore, we propose that the rate of increase in saturation photocurrent depends on the number of energy states that the electrons (holes) can access in the conduction (valence) band which depend on the photon energy that they absorbed and the energy level of the defect states in the bandgap where the electrons (holes) are initially trapped.

To capture the net effect of these competing mechanisms, a logistic equation was used to model the impact of excitation intensity on the saturation photocurrent in a single ZnO-NS at steady state, i.e.

$$\frac{\mathrm{d}J_{sat}}{\mathrm{d}I} = aJ_{sat} - bJ_{sat}{}^2. \tag{6}$$

The first term in the right-hand side of equation (6) accounts for the generation of electron–hole pairs, while the second term limits the concentration of electrons (holes) in populating the conduction (valence) band. The ratio of a and b is the steady state value of the saturated photocurrent with respect to the excitation intensity. The general solution of equation (6) is

$$J_{sat}(I) = \frac{a}{b + J_o e^{-r(I-I_o)}}, \tag{7}$$

where I_o is the initial intensity of the light source, $J_o = J(I_o)$ is the initial photocurrent density, and r is the rate of rise of the saturation photocurrent with intensity, I. Note that equation (7) will plateau at a specific illumination intensity. One can understand the saturation in terms of the density of initial states that the energy of the illumination source can access and excite into the CB, and because the number density of electrons in a given state is finite, the contribution to the current density from any given initial state will saturate. Note that the density of electrons in different initial states varies from state to state. While recombination, traps, etc affect the saturation current, we can safely assume that the density of initial states accessible with a given illumination source sets the upper limit on the saturation current density, J_{sat}. Consequently, the contribution of individual initial states or bands of states to the current density will saturate at different intensities of the illumination source. When this happens, a break in the photocurrent density is observed. In the case of 532 and 633 nm excitation, a single break is observed within the range of the excitation intensity used in this study. This suggests that at a minimum, there are two bands of states that these sources access and excite to the CB. Because the probability of a transition is a function of the scattering cross section, which depends on the wavelength of light, and the initial and final state bands of the transition, we must assume that two bands of initial states accessed with 532 and 633 nm excitation are not necessarily the same. In fact, it is to be expected given that the 532 nm excitation source can access a larger energy range of initial states compared to 633 nm excitation, which is evident from the larger photocurrent with 532 nm excitation in figure 3.

In contrast to 532 and 633 nm excitation, two breaks are observed in the normalized saturation photocurrent density versus intensity profile with 405 nm excitation, as shown in figure 6(a). This is to be expected given that the energy of the photons is 3.06 eV and nearly spans the ZnO bandgap of 3.37 eV. Clearly, a large range of initial states are accessed using the 405 nm excitation source, which is supported by the largest photocurrent (figure 3) of the three excitation sources used in this study. Consequently, the saturation photocurrent versus excitation intensity curve for 405 nm of the single ZnO-NS can be fitted with the sum of three different logistic functions of the form of equation (7):

$$J_{\text{tot}} = J_1 + J_2 + J_3 = \sum_i \frac{a_i}{b_i + J_{\text{o},i} e^{-r_i(I-I_o)}}. \quad (8)$$

The results of the fit with equation (8) is displayed in figure 7. The extracted parameters for the 405 nm excitation source are $a_i = (3.5, 5.1, 7.1)$, $b_i = (1.2, 1.3, 1.4)$, $J_{\text{o},i} = (1.9, 2.0, 3.9)$, and $r_i = (46, 5.2, 3.0)$ for J_1, J_2, and J_3, respectively. The fit indicates that each ratio of a_i and b_i pertains to the different transition levels of electrons (holes) from a given defect state in the bandgap to the conduction (valence) band. Here, $J_{\text{o},i}$ is a function of the number of electrons (holes) that are involved in the transition to populate the conduction (valence) band, and r_i relates to the recombination rate of electrons and holes, where higher r may be an indication of slower recombination rates.

6. Conclusions

The electrical and photoconductive properties of a single ZnO-NS were analyzed with near-UV and sub-bandgap excitation sources and display a typical two-step fast and slow rise and decay photocurrent behavior, similarly observed in other ZnO materials. The physical models used to describe the two-step rise and decay photocurrent characteristics show that these behaviors are highly dependent upon the excitation energy, the depths of the NPDs, and the subsequent trapping of electrons and holes during and after excitation. Significant hole trapping with the 532 nm excitation source is attributed as the source of the observed long photocurrent rise time during illumination and the strong persistence in the photocurrent following termination of illumination, where trapped holes are unable to facilitate desorption of surface oxygen and the corresponding high potential barrier increases the electron lifetime in the CB. The energy levels of the trap depths for each excitation source were estimated from the photoconductive decay data and show that shallow level traps are vacated before deep level traps, and that the depth of the deep level traps during the slow portion of photoconductive decay at ~0.9 eV closely matches the reported energy levels of singly and doubly ionized oxygen vacancies, which have previously been shown to be responsible for hole trapping in ZnO. Use of a phenomenological model shows that the saturation photocurrent versus excitation intensity profile can be fit with a sum of logistic functions with each curve representing different recombination rates and transitions from different defect states in the bandgap. We find that the slopes of the saturation photocurrent versus excitation intensity dependence profile are a function of the transition probabilities of defect states, the number of carriers available to populate the conduction (valence) band, and the rate at which electrons and holes recombine. This work demonstrates the utility of a ZnO-coated silica NS for obtaining detailed information about defect states in ZnO. Finally, this study demonstrates the value of constructing similar core–shell one-dimensional nanostructured devices with other materials to uncover detailed electronic properties of materials.

Acknowledgments

The authors would like to acknowledge the Office of Naval Research (Grant #: N00014-20-1-2433) for their support of this work.

ORCID iDs

Peter M Wojcik https://orcid.org/0000-0002-2125-5702
Lyndon D Bastatas https://orcid.org/0000-0003-1199-9676

References

[1] Soci C, Zhang A, Xiang B, Dayeh S A, Aplin D P R, Park J, Bao X Y, Lo Y H and Wang D 2007 ZnO nanowire UV photodetectors with high internal gain *Nano Lett.* **7** 1003–9
[2] Kind H, Yan H, Messer B, Law M and Yang P 2002 Nanowire ultraviolet photodetectors and optical switches *Adv. Mater.* **14** 158–60
[3] Yuan J, Hu L, Xu Z, Zhang Y, Li H, Cao X, Liang H, Ruan S and Zeng Y-J 2019 Concurrent improvement of photocarrier separation and extraction in ZnO nanocrystal ultraviolet photodetectors *J. Phys. Chem.* C **123** 14766–73
[4] Khokhra R, Bharti B, Lee H-N and Kumar R 2017 Visible and UV photo-detection in ZnO nanostructured thin films via simple tuning of solution method *Sci. Rep.* **7** 15032
[5] Deka Boruah B 2019 Zinc oxide ultraviolet photodetectors: rapid progress from conventional to self-powered photodetectors *Nanoscale Adv.* **1** 2059–85
[6] Chou J-C, Ko C-C, Kuo P-Y, Lai C-H, Nien Y-H and Chang J-X 2019 Fabrication of dye-sensitized solar cells using zinc oxide nanorod-modified titanium dioxide photoanode *IEEE Trans. Nanotechnol.* **18** 553–61
[7] Tiwana P, Docampo P, Johnston M B, Snaith H J and Herz L M 2011 Electron mobility and injection dynamics in mesoporous ZnO, SnO_2, and TiO_2 films used in dye-sensitized solar cells *ACS Nano* **5** 5158–66
[8] Bastatas L, Wagle P, Echeverria E, Austin A and McIlroy D 2019 The effect of UV illumination on the room temperature detection of vaporized ammonium nitrate by a ZnO coated nanospring-based sensor *Materials* **12** 302
[9] Bakharev P and McIlroy D 2015 Signal-to-noise enhancement of a nanospring redox-based sensor by lock-in amplification *Sensors* **15** 13110–20
[10] Bakharev P V and McIlroy D N 2014 The effect of the periodic boundary conditions of a ZnO-coated nanospring on its

surface redox-induced electrical response *Nanotechnology* **25** 475501
[11] Dobrokhotov V *et al* 2012 ZnO coated nanospring-based chemiresistors *J. Appl. Phys.* **111** 044311
[12] Liang H, Feng Q, Xia X, Li R, Guo H, Xu K, Tao P, Chen Y and Du G 2014 Room temperature electroluminescence from arsenic doped p-type ZnO nanowires/n-ZnO thin film homojunction light-emitting diode *J. Mater. Sci., Mater. Electron.* **25** 1955–8
[13] Son D I, Kwon B W, Park D H, Seo W-S, Yi Y, Angadi B, Lee C-L and Choi W K 2012 Emissive ZnO–graphene quantum dots for white-light-emitting diodes *Nat. Nanotechnol.* **7** 465–71
[14] Zhang L, Bai S, Su C, Zheng Y, Qin Y, Xu C and Wang Z L 2015 A high-reliability kevlar fiber-ZnO nanowires hybrid nanogenerator and its application on self-powered UV detection *Adv. Funct. Mater.* **25** 5794–8
[15] Wang J, Chen R, Xiang L and Komarneni S 2018 Synthesis, properties and applications of ZnO nanomaterials with oxygen vacancies: a review *Ceram. Int.* **44** 7357–77
[16] Bora T, Zoepfl D and Dutta J 2016 Importance of plasmonic heating on visible light driven photocatalysis of gold nanoparticle decorated zinc oxide nanorods *Sci. Rep.* **6** 26913
[17] Cammi D *et al* 2018 Enhancement of the sub-band-gap photoconductivity in ZnO nanowires through surface functionalization with carbon nanodots *J. Phys. Chem.* C **122** 1852–9
[18] Kouklin N 2008 Cu-doped ZnO nanowires for efficient and multispectral photodetection applications *Adv. Mater.* **20** 2190–4
[19] Prabhakar R R, Mathews N, Jinesh K B, Karthik K R G, Pramana S S, Varghese B, Sow C H and Mhaisalkar S 2012 Efficient multispectral photodetection using Mn doped ZnO nanowires *J. Mater. Chem.* **22** 9678
[20] Hu L *et al* 2019 Defect reconstruction triggered full-color photodetection in single nanowire phototransistor *ACS Photonics* **6** 886–94
[21] Moazzami K, Murphy T E, Phillips J D, Cheung M C-K and Cartwright A N 2006 Sub-bandgap photoconductivity in ZnO epilayers and extraction of trap density spectra *Semicond. Sci. Technol.* **21** 717–23
[22] Bastatas L D, Wagle P, Echeverria E, Slinker J D and McIlroy D N 2019 Electrical characterization of ZnO-coated nanospring ensemble by impedance spectroscopy: probing the effect of thermal annealing *Nanotechnology* **30** 234006
[23] Kavitha M K, Jinesh K B, Philip R, Gopinath P and John H 2014 Defect engineering in ZnO nanocones for visible photoconductivity and nonlinear absorption *Phys. Chem. Chem. Phys.* **16** 25093–100
[24] Alenezi M R, Henley S J and Silva S R P 2015 On-chip fabrication of high performance nanostructured ZnO UV detectors *Sci. Rep.* **5** 8516
[25] Ye J D *et al* 2005 Correlation between green luminescence and morphology evolution of ZnO films *Appl. Phys.* A **81** 759–62
[26] Bandopadhyay K and Mitra J 2015 Zn interstitials and O vacancies responsible for n-type ZnO: what do the emission spectra reveal? *RSC Adv.* **5** 23540–7
[27] Sett D, Sarkar S and Basak D 2014 A successive photocurrent transient study to probe the sub-band gap electron and hole traps in ZnO nanorods *RSC Adv.* **4** 58553–8
[28] Ahn C H, Kim Y Y, Kim D C, Mohanta S K and Cho H K 2009 A comparative analysis of deep level emission in ZnO layers deposited by various methods *J. Appl. Phys.* **105** 013502
[29] Lima S A M, Sigoli F A, Jafelicci M Jr and Davolos M R 2001 Luminescent properties and lattice defects correlation on zinc oxide *Int. J. Inorg. Mater.* **3** 749–54
[30] Clark S J, Robertson J, Lany S and Zunger A 2010 Intrinsic defects in ZnO calculated by screened exchange and hybrid density functionals *Phys. Rev.* B **81** 115311
[31] Janotti A and Van de Walle C G 2006 New insights into the role of native point defects in ZnO *J. Cryst. Growth* **287** 58–65
[32] Bandopadhyay K and Mitra J 2016 Spatially resolved photoresponse on individual ZnO nanorods: correlating morphology, defects and conductivity *Sci. Rep.* **6** 28468
[33] Fan Z, Chang P, Lu J G, Walter E C, Penner R M, Lin C and Lee H P 2004 Photoluminescence and polarized photodetection of single ZnO nanowires *Appl. Phys. Lett.* **85** 6128–30
[34] Keem K, Kim H, Kim G-T, Lee J S, Min B, Cho K, Sung M-Y and Kim S 2004 Photocurrent in ZnO nanowires grown from Au electrodes *Appl. Phys. Lett.* **84** 4376–8
[35] Li Q H, Gao T, Wang Y G and Wang T H 2005 Adsorption and desorption of oxygen probed from ZnO nanowire films by photocurrent measurements *Appl. Phys. Lett.* **86** 123117
[36] Liu Y *et al* 2009 Visible light response of unintentionally doped ZnO nanowire field effect transistors *J. Phys. Chem.* C **113** 16796–801
[37] Menzel A, Subannajui K, Güder F, Moser D, Paul O and Zacharias M 2011 Multifunctional ZnO-nanowire-based sensor *Adv. Funct. Mater.* **21** 4342–8
[38] Reemts J and Kittel A 2007 Persistent photoconductivity in highly porous ZnO films *J. Appl. Phys.* **101** 013709
[39] Mishra S K, Srivastava R K, Prakash S G, Yadav R S and Panday A C 2010 Photoluminescence and photoconductive characteristics of hydrothermally synthesized ZnO nanoparticles *Opto-Electron. Rev.* **18** 467–73
[40] Covington L R and Moore J C 2013 Photoconductivity and transient response of Al:ZnO:Al planar structures fabricated via a thermal oxidation process *Thin Solid Films* **540** 106–11
[41] Jin Y, Wang J, Sun B, Blakesley J C and Greenham N C 2008 Solution-processed ultraviolet photodetectors based on colloidal ZnO nanoparticles *Nano Lett.* **8** 1649–53
[42] Sharma P, Sreenivas K and Rao K V 2003 Analysis of ultraviolet photoconductivity in ZnO films prepared by unbalanced magnetron sputtering *J. Appl. Phys.* **93** 3963–70
[43] Dhara S and Giri P 2011 Enhanced UV photosensitivity from rapid thermal annealed vertically aligned ZnO nanowires *Nanoscale Res. Lett.* **6** 504
[44] Hasan Farooqi M M and Srivastava R K 2017 Structural, optical and photoconductivity study of ZnO nanoparticles synthesized by annealing of ZnS nanoparticles *J. Alloys Compd.* **691** 275–86
[45] Prades J D, Hernandez-Ramirez F, Jimenez-Diaz R, Manzanares M, Andreu T, Cirera A, Romano-Rodriguez A and Morante J R 2008 The effects of electron–hole separation on the photoconductivity of individual metal oxide nanowires *Nanotechnology* **19** 465501
[46] Bao J, Shalish I, Su Z, Gurwitz R, Capasso F, Wang X and Ren Z 2011 Photoinduced oxygen release and persistent photoconductivity in ZnO nanowires *Nanoscale Res. Lett.* **6** 404
[47] Cammi D and Ronning C 2014 Persistent photoconductivity in ZnO nanowires in different atmospheres *Adv. Condens. Matter Phys.* **2014** 1–5
[48] Wang Y, Liao Z, She G, Mu L, Chen D and Shi W 2011 Optical modulation of persistent photoconductivity in ZnO nanowires *Appl. Phys. Lett.* **98** 203108
[49] Zong X-L and Zhu R 2015 Effects of surface adsorbed oxygen, applied voltage, and temperature on UV photoresponse of ZnO nanorods *Chin. Phys.* B **24** 107703
[50] Wojcik P M, Bakharev P V, Corti G and McIlroy D N 2017 Nucleation, evolution, and growth dynamics of amorphous silica nanosprings *Mater. Res. Express* **4** 015004

[51] Wang L, Major D, Paga P, Zhang D, Norton M G and McIlroy D N 2006 High yield synthesis and lithography of silica-based nanospring mats *Nanotechnology* **17** S298–303

[52] Corti G, Brown J, Rajabi N and McIlroy D N 2018 Threefold growth efficiency improvement of silica nanosprings by using silica nanosprings as a substrate *Nanotechnology* **29** 115604

[53] Rajabi N, Wojcik P M, Khanal L R, Qiang Y and McIlroy D N 2018 A comparison of the morphological and electrical properties of sol-gel dip coating and atomic layer deposition of ZnO on 3D nanospring mats *Mater. Res. Express* **6** 035902

[54] Schmidt-Mende L and MacManus-Driscoll J L 2007 ZnO—nanostructures, defects, and devices *Mater. Today* **10** 40–8

[55] McCluskey M D 2018 Defects in ZnO *Defects in Advanced Electronic Materials and Novel Low Dimensional Structures* (Amsterdam: Elsevier) pp 1–25

[56] Özgür Ü, Alivov Y I, Liu C, Teke A, Reshchikov M A, Doğan S, Avrutin V, Cho S-J and Morkoç H 2005 A comprehensive review of ZnO materials and devices *J. Appl. Phys.* **98** 041301

[57] McCluskey M D and Jokela S J 2009 Defects in ZnO *J. Appl. Phys.* **106** 071101

[58] Vlasenko L S and Watkins G D 2005 Optical detection of electron paramagnetic resonance in room-temperature electron-irradiated ZnO *Phys. Rev.* B **71** 125210

[59] Alvi N H, ul Hasan K, Nur O and Willander M 2011 The origin of the red emission in n-ZnO nanotubes/p-GaN white light emitting diodes *Nanoscale Res. Lett.* **6** 130

[60] Xu P S, Sun Y M, Shi C S, Xu F Q and Pan H B 2003 The electronic structure and spectral properties of ZnO and its defects *Nucl. Instrum. Methods Phys. Res.* B **199** 286–90

[61] Lin B, Fu Z and Jia Y 2001 Green luminescent center in undoped zinc oxide films deposited on silicon substrates *Appl. Phys. Lett.* **79** 943–5

[62] Tam K H *et al* 2006 Defects in ZnO nanorods prepared by a hydrothermal method *J. Phys. Chem.* B **110** 20865–71

[63] An W, Wu X and Zeng X C 2008 Adsorption of O_2, H_2, CO, NH_3, and NO_2 on ZnO nanotube: a density functional theory study *J. Phys. Chem.* C **112** 5747–55

[64] Safa S, Khajeh M and Azimirad R 2018 The effects of measuring atmosphere on ultraviolet photodetection performance of ZnO nanostructures *J. Alloys Compd.* **735** 1406–13

[65] Purusothaman Y, Alluri N R, Chandrasekhar A, Vivekananthan V and Kim S-J 2018 Regulation of charge carrier dynamics in ZnO microarchitecture-based UV/Visible photodetector via photonic-strain induced effects *Small* **14** 1703044

[66] Chen R-S, Wang W-C, Chan C-H, Hsu H-P, Tien L-C and Chen Y-J 2013 Photoconductivities in monocrystalline layered V_2O_5 nanowires grown by physical vapor deposition *Nanoscale Res. Lett.* **8** 443

[67] Watanabe H, Wada M and Takahashi T 1965 The activation energy for oxygen desorption from zinc oxide surfaces *Japan. J. Appl. Phys.* **4** 945–7

[68] Carrey J, Carrère H, Kahn M L, Chaudret B, Marie X and Respaud M 2008 Photoconductivity of self-assembled ZnO nanoparticles synthesized by organometallic chemistry *Semicond. Sci. Technol.* **23** 025003

[69] Worasawat S, Tasaki K, Neo Y, Pecharapa W, Hatanaka Y and Mimura H 2019 Persistent photocurrent characteristics of ZnO polycrystalline films prepared by RF magnetron sputtering *Japan. J. Appl. Phys.* **58** 055505

[70] Moore J and Thompson C 2013 A phenomenological model for the photocurrent transient relaxation observed in ZnO-based photodetector devices *Sensors* **13** 9921–40

[71] Madel M, Huber F, Mueller R, Amann B, Dickel M, Xie Y and Thonke K 2017 Persistent photoconductivity in ZnO nanowires: influence of oxygen and argon ambient *J. Appl. Phys.* **121** 124301

[72] Collins R J and Thomas D G 1958 Photoconduction and surface effects with zinc oxide crystals *Phys. Rev.* **112** 388–95

[73] Melnick D A 1957 Zinc oxide photoconduction, an oxygen adsorption process *J. Chem. Phys.* **26** 1136–46

[74] Lany S and Zunger A 2005 Anion vacancies as a source of persistent photoconductivity in II–VI and chalcopyrite semiconductors *Phys. Rev.* B **72** 035215

[75] Mallampati B, Nair S V, Ruda H E and Philipose U 2015 Role of surface in high photoconductive gain measured in ZnO nanowire-based photodetector *J. Nanopart. Res.* **17** 176

[76] Lee J-M, Kim K-K, Park S-J and Choi W-K 2001 Low-resistance and nonalloyed ohmic contacts to plasma treated ZnO *Appl. Phys. Lett.* **78** 3842–4

[77] Chen J-J, Jang S, Anderson T J, Ren F, Li Y, Kim H-S, Gila B P, Norton D P and Pearton S J 2006 Low specific contact resistance Ti/Au contacts on ZnO *Appl. Phys. Lett.* **88** 122107

[78] Kim H-K, Bae J W, Kim K-K, Park S-J, Seong T-Y and Adesida I 2004 Inductively-coupled-plasma reactive ion etching of ZnO using BCl_3-based plasmas and effect of the plasma treatment on Ti/Au ohmic contacts to ZnO *Thin Solid Films* **447–448** 90–4

[79] Murphy T E, Blaszczak J O, Moazzami K, Bowen W E and Phillips J D 2005 Properties of electrical contacts on bulk and epitaxial n-type ZnO *J. Electron. Mater.* **34** 389–94

[80] Heiland G, Mollwo E and Stöckmann F 1959 Electronic processes in zinc oxide *Solid State Physics* vol 8 (Amsterdam: Elsevier) pp 191–323

[81] Takahashi Y, Kanamori M, Kondoh A, Minoura H and Ohya Y 1994 Photoconductivity of ultrathin zinc oxide films *Japan. J. Appl. Phys.* **33** 6611–5

[82] Razavi-Khosroshahi H *et al* 2017 High-pressure zinc oxide phase as visible-light-active photocatalyst with narrow band gap *J. Mater. Chem.* A **5** 20298–303

[83] Lee H, An N, Jeong S, Kang S, Kwon S, Lee J, Lee Y, Kim D Y and Lee S 2017 Strong dependence of photocurrent on illumination-light colors for ZnO/graphene Schottky diode *Curr. Appl. Phys.* **17** 552–6

[84] Penfold T J *et al* 2018 Revealing hole trapping in zinc oxide nanoparticles by time-resolved x-ray spectroscopy *Nat. Commun.* **9** 478

[85] Tian Y, Zhang J, Guo C F, Zhang B and Liu Q 2016 Photoconductive probing of the trap distribution in switchable interfaces *Nanoscale* **8** 915–20

[86] Bube R H 1978 *Photoconductivity of Solids* (Huntington, NY: R.E. Krieger Pub. Co)

[87] Randall J T and Wilkins M H F 1945 Phosphorescence and electron traps: I. The study of trap distributions *Proc. R. Soc.* A **184** 365–89

[88] Rose A 1963 *Concepts in Photoconductivity and Allied Problems* (New York: Interscience Publishers)

[89] Pillai P K C, Shroff N, Kumar N N and Tripathi A K 1985 Photoconductivity and dark-conductivity studies of $CdS_{1-x}Se_x$ (Cu) sintered layers *Phys. Rev.* B **32** 8228–33